

are often discussed in the context of stirring and stretching (Bergantz, 2000; Perugini *et al.*, 2003; Ruprecht *et al.*, 2008); however, homogenisation on all scales requires diffusive exchange along chemical gradients, especially in magma reservoirs with limited convection (Pichavant *et al.*, 2007). These mixing systems are typically characterised by multi-phase (crystal + melt + fluid) sub-liquidus conditions. To date, few experiments have explored the complex interplay of diffusion and phase change(s) at sub-liquidus temperatures (*e.g.*, Watson, 1982; Pistone *et al.*, 2016).

A magma mixing redox trap that moderates mass transfer of sulphur and metals

A. Fiege^{1,2*}, P. Ruprecht³, A. Simon¹



Abstract

doi: 10.7185/geochemlet.1722

Mixing and juxtaposition of chemically distinct magmatic systems are key processes for the evolution of Earth's crust. Yet, the physicochemical nature at mixing interfaces remains poorly described, as crystallisation, melting, heat transfer, and diffusion are interconnected and lead to complex mass transfer processes driving unique patterns of element fractionation. Here, we use diffusion couple experiments between felsic and mafic magmas (melt + crystals ± volatiles) to document the formation of large gradients in oxygen fugacity at the magma-magma mixing interface. Reducing and oxidising boundary layers at the interface develop rapidly and remain in dynamic disequilibrium for days to possibly weeks. We suggest that the observed transient redox gradient is caused by cation transfer across the interface where the required counter flux of electron holes is insufficient to compensate an evolving electron hole gradient. Such boundary layer redox effects may control fractionation of polyvalent and chalcophile elements and moderate, for example, Cu/Au ratios in arc-related porphyry ore deposits.

Received 26 October 2016 | Accepted 29 March 2017 | Published 15 May 2017

Introduction and Approach

Magmatic systems in Earth's crust evolve through interplay between magma supply from the mantle and magma withdrawal feeding shallow reservoirs and, ultimately, volcanic eruptions (DePaolo, 1981; Hildreth and Moorbath, 1988; Annen *et al.*, 2006). As a consequence, magma mixing is ubiquitous (Bacon and Metz, 1984; Ruprecht and Bachmann, 2010) and frequently invoked to explain geochemical records of, for example, volcanic gases (Wallace and Gerlach, 1994) and porphyry ore deposits (Audétat and Simon, 2012). Magma mixing processes

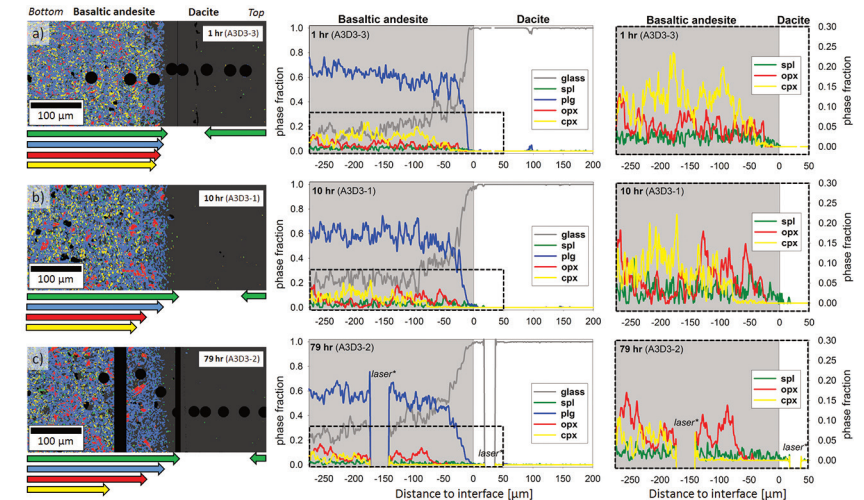


Figure 1 Maps and phase fraction plots illustrating the phase assemblages of the run products. The experiments were run vertically (top: dacite; bottom: basaltic andesite). **(a)** 1 hr run (experiment A3D3-3). **(b)** 10 hr (A3D3-1); **(c)** 79 hr (A3D3-2). *Left column*: WDS (Al, Fe, Mg, Ca, K) and EDS (Si, Na) maps were used to produce phase assemblage maps. The “glass only” area (grey) of each diffusion couple grows with time. The arrows below each map indicate the presence of a certain mineral phase away from the basaltic andesite or dacitic far side up until the tip of the respective arrow, where green = spinel (spl), blue = plagioclase (plg), red = orthopyroxene (opx), and yellow = clinopyroxene (cpx). *Centre and right column*: The phase fraction for a certain distance away from the interface was calculated using WDS/EDS maps. The right column is a magnification, displaying only the fractions for spl, opx, and cpx. *Position of the vertical laser-ablation transect. For IGSN sample registration see Supplementary Information. Phase fractions are provided in Supplementary Information D.

We performed sub-liquidus time-series experiments in rapid-quench, cold-seal TZM pressure vessels, which were investigated by micro X-ray absorption near-edge structure (μ -XANES) spectroscopy at Fe K-edge (Fiege *et al.*, 2017), and two-oxide oxybarometry (Ghiorso and Evans, 2008), to document redox evolution near the magma-magma interface. Hydrous basaltic andesite and dacite cylinders were equilibrated separately at different conditions in gold capsules (basaltic andesite: 1030 °C, 1.1 wt. % H₂O, 1000 ppm S, 500 ppm Cl;

1. Earth and Environmental Sciences, University of Michigan, 1100 North University Ave, Ann Arbor, MI 48109-1005, USA
2. Earth and Planetary Sciences, American Museum of Natural History, Central Park West at 79th Street, New York, NY 10024-5192, USA
- * Corresponding author (email: afiege@amnh.org)
3. Geological Sciences & Engineering, University of Nevada, 1664 N. Virginia Street, Reno, NV 89557, USA



dacite: 950 °C, 3.9 wt. % H₂O, 100 ppm S, 1500 ppm Cl; both at QFM + 4 and 150 MPa). The capsules were sliced, polished, and loaded into a gold capsule with the basaltic andesite on bottom and the dacite on top. The capsules were sealed with a lid on bottom and star crimped on top. Pre-compression of the capsules (~100 MPa) resulted in an ideal planar contact between both cylinders due to the star crimping technique. Subsequent mixing experiments (1000 °C, 150 MPa, QFM + 4, 1 to 79 hr) reveal a mostly crystal-free dacite. Minor amounts of Fe-Ti-oxides are consumed with time in a growing oxide-free zone near the interface (~50 to ~150 μm wide; Fig. 1). Meanwhile, crystallinity of the basaltic andesite near the interface (<150 μm) decreases continuously with time. During the mixing process, clinopyroxene (cpx) is the first completely resorbed silicate phase, followed by orthopyroxene (opx). Plagioclase (plg) is resorbed significantly near the interface in all experiments, but continues to constitute a rigid crystal network throughout the basaltic andesite. With increasing run duration, concentrations of felsic and mafic components decrease and increase, respectively, in the dacitic melt near the interface (Fig. S-A3). Diffusion profiles were observed for S (mafic to felsic) and Cl (felsic to mafic), whereas H₂O remains constant away from the interface (Supplementary Information A and C).

Determination of Redox Profiles

Redox-sensitive oxide-pairs (ilmenite, il; and spinel, spl) in the basaltic andesite reveal systematic compositional variations (Fig. 2, Table S-C9); the dacite lacks il, which prevents the application of two-oxide oxybarometry. In 1 hr and 10 hr experiments, X_{il} (fraction of FeTiO₃ in il) and X_{uv} (fraction of TiFe₂O₄ in spl) decrease from ~0.45 and ~0.15 in the basaltic andesite far field to ~0.33 and ~0.10 near the interface, respectively. Far field oxide compositions are similar to those in the starting basaltic andesite (X_{il} ~0.44; X_{uv} ~0.13). The 79 hr experiment shows a more evolved profile, wherein the basaltic andesite interior contains oxides with compositions similar to the 1 hr and 10 hr experiment. A broad (>1500 μm) continuous decrease in X_{il} (~0.42 to ~0.24) and X_{uv} (~0.11 to ~0.05) emerges towards the interface. In contrast to the 1 hr and 10 hr profile, a decrease in X_{il} (~0.34) and X_{uv} (~0.06) was measured in the basaltic andesite far field (>2500 μm), which is directly related to the fO_2 imposed by the experimental apparatus; *i.e.* an effect not expected in natural systems (see Supplementary Information A). These length scales of X_{il} and X_{uv} variations are significantly larger than the measured changes in crystallinity (<150 μm; Fig. 1), indicating that the observed redox gradient is largely decoupled from crystal resorption rate.

The μ-XANES analyses of the dacitic glass reveal significant changes in Fe oxidation state (Fig. 2b, Tables S-C11 to S-C13) that correlate spatially with FeO_{tot} and other melt constituents (Fig. 2b,d). In the 1 hr and 10 hr experiments, Fe³⁺/ΣFe of the dacitic melt decreases by ~23 % from the far field to the interface. The Fe redox profile is relatively flat at 79 hr, with a minor decrease of Fe³⁺/ΣFe

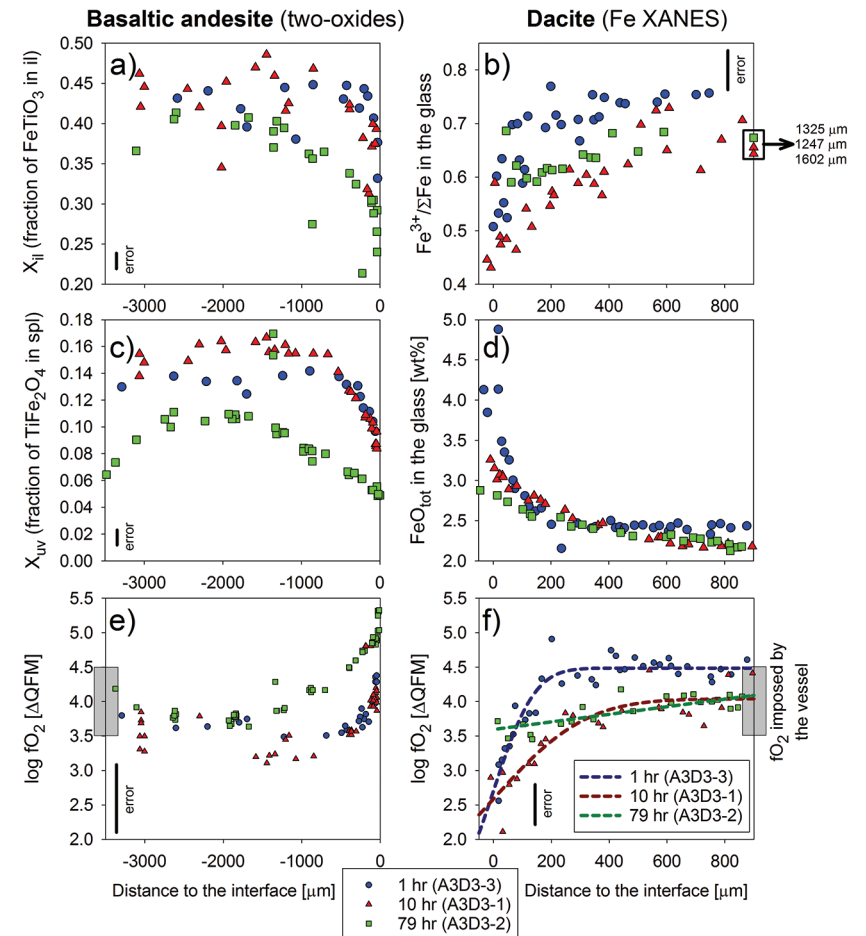


Figure 2 Redox profiles in the dacite and the basaltic andesite determined by Fe μ-XANES and two-oxide oxybarometry, respectively. (a) Fraction of TiFe₂O₄ in spl vs. distance to the interface. (b) Fe³⁺/ΣFe in dacitic glass vs. distance to the interface. (c) Fraction of FeTiO₃ in il vs. distance to the interface. (d) FeO_{tot} concentrations in the melt on the dacitic side. (e) fO_2 of the basaltic andesite side vs. distance to the interface; fO_2 was calculated using Ghiorso and Evans (2008). (f) fO_2 of the dacite side vs. distance to the interface; fO_2 was predicted using Moretti (2005). For the calculations we used the Fe³⁺/ΣFe ratios determined via XANES and the local glass composition determined via EPMA (Supplementary Information A). The vertical black bars represent the average of 2σ errors (Fig. 2a-c); 1σ error of the FeO_{tot} concentrations in the glasses is ±0.2 wt. % (Fig. 2d). The indicated errors for fO_2 represent conservative estimations for the overall uncertainty of the two-oxides (±0.5 log units; Fig. 2e) and Fe μ-XANES (±0.2 log units; Fig. 2f) method, respectively. Both methods reproduce the fO_2 imposed by the vessel within 0.2 log units for run duration ≥10 hr, providing an independent constraint for the high accuracy and comparability of the two datasets.



from ~68 % in the far field to ~60 % near the interface. At 200 μm (1 hr run) and 500 μm (10 hr and 79 hr) away from the interface, the profiles remain at constant $\text{Fe}^{3+}/\Sigma\text{Fe}$, whereas the far field of the 1 hr experiments is characterised by a ~6 % higher $\text{Fe}^{3+}/\Sigma\text{Fe}$ compared to the 10 hr and 79 hr runs. The 6 % difference likely results from juxtaposing hotter mafic and cooler felsic magma at intermediate mixing temperatures, simulating nature. Here, fast thermal equilibration decreases $\text{Fe}^{3+}/\Sigma\text{Fe}$ in the cooling mafic melt fraction and increases $\text{Fe}^{3+}/\Sigma\text{Fe}$ within the heating felsic melt. This is confirmed by the far field results (Fig. 2), whereas the buffering capacity of the vessel eliminates this temperature effect with increasing run duration. The small quenched melt pools on the mafic side precluded precise XANES analyses.

Models for $\text{Fe}^{3+}/\Sigma\text{Fe}$ (Fiege *et al.*, 2017) and two-oxide oxybarometry (Ghiorso and Evans, 2008) reveal a zigzag redox trend near the interface (Fig. 2e-f). In particular, we observe a sudden $f\text{O}_2$ drop at the interface that increases from ~1.3 log units $f\text{O}_2$ after 1 hr and 10 hr to ~1.8 log units $f\text{O}_2$ after 79 hr. Considering the temperature effect on $f\text{O}_2$, the far sides of the longest run provide the best estimation of the accuracy of the two methods; *i.e.* both methods reproduce the local $f\text{O}_2$ within 0.2 log units, considering the $f\text{O}_2$ imposed by the vessel (QFM + 4; see Fig. 2e,f and Supplementary Information A.4.4). The oxide pairs are within $\leq 50 \mu\text{m}$ of each other relative to the interface and we only considered oxide pairs in Mg/Mn equilibrium (Bacon and Hirschmann, 1988).

Discussion of the Redox Mechanism

Intriguingly, a significant redox gradient at the interface is observed in all run products, reaching ~1.8 log units $f\text{O}_2$ after 79 hr. Thus, this transient redox gradient may initially grow with time and is of relevance for several days and possibly weeks. In the absence of water diffusion profiles (confirmed by Raman spectroscopy on the dacitic side; see Supplementary Information C), water exchange cannot be responsible for the redox gradient. In magmatic systems, the net redox gradient at the interface may grow with time, considering that our experiments are externally buffered, resulting in a fading redox gradient with increasing run duration, consistent with H_2 diffusivities (see Zhang and Ni, 2010; and Supplementary Information A.4.5).

We propose that the redox gradient reflects a transient electron hole gradient that emerges between two mixing magmas as mass is transferred across the interface. The observed mineral resorption sequence of $\text{cpx} \rightarrow \text{opx} \rightarrow \text{plg}$ (\rightarrow oxides; Fig. 1) and concentration maxima at the interface for, *e.g.*, Fe and Mg (Fig. S-A3) indicate that compatible elements are added to the melt near the interface, inducing a diffusive flux from mafic to felsic magma. Mass transfer of cations, and, in particular, of divalent network modifying cations, requires a counter flux of charge-compensating electron holes (h^* , where the superscript dot indicates a single positive charge), which are the dominant mobile electronic species in Fe-bearing silicate melts (*e.g.*, Cooper *et al.*, 2010; Cooper, 2017).

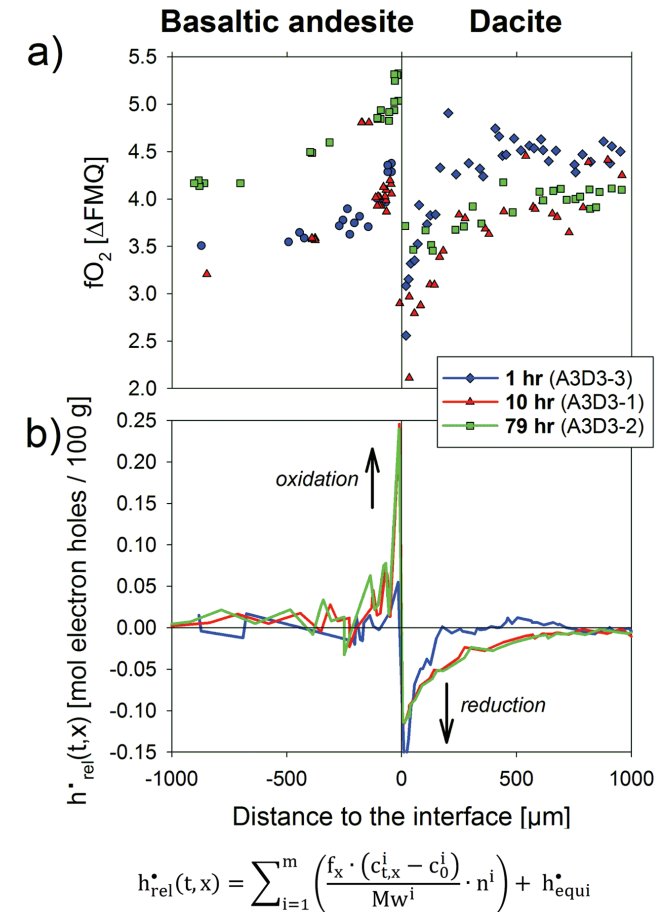


Figure 3 Diffusion-induced redox gradients and estimate of the electron hole disequilibrium of the melt across the interface. (a) Magnification of Figure 2e-f. (b) The trends are calculated using the equation below the figure, where $h^*_{\text{rel}}(t,x)$ is the relative change in electron holes (mol/100 g) at a distance x to the interface and at a time t integrated diffusive flux, thus, the sum of the concentration differences for each element i with the oxidation state n (*e.g.*, $n = +1$ for Na and $n = -1$ for Cl) from its initial concentration ($c_{t,x} - c_0$). Mw and $f_{t,x}$ are the molecular weight and the melt fraction, respectively. The melt composition at the far side of the basaltic andesite and the dacite was assumed to represent the zero-time melt composition (c_0). The calculated trends probably represent the maximum diffusion-induced electron hole gradient because we do not account for the effects of simultaneous electron hole equilibration (h^*_{equi}), associated, *e.g.*, with h^* counter flux, H_2 diffusion, and phase change (*i.e.* mineral dissolution); the latter process is presumably balanced, whereas the first two compensate h^* gradients with time. The calculated h^* gradients would allow the oxidation/reduction of up to 10 wt. % Fe near the interface, while we observe a maximum change by ~0.8 wt. % Fe (see Supplementary Information A.4.5).



This coupled *cation - electron hole* flux in Fe-bearing silicate melts (Mode III redox; Cook and Cooper, 2000) kinetically dominates redox control relative to other known mechanisms that involve flux of a neutral gas species (*e.g.*, Mode I of Cook and Cooper, 2000; see also Gaillard *et al.*, 2003) and oxygen flux (*e.g.*, Mode II of Cook and Cooper, 2000); the latter mechanism has mostly been ruled out as a diffusive redox control in silicate melts (Cooper *et al.*, 1996; Gaillard *et al.*, 2003).

In a magma-magma mixing environment, the thermodynamic disequilibrium imposed by juxtaposing two chemically distinct systems results in a chemical potential that drives significant mass transfer between both systems (*e.g.*, see Fig. S-A3). Thus, the formation of a redox gradient at a magma-magma interface suggests that the h^{\bullet} counter flux is insufficient to balance the significant mass flux across the interface, indicating rather low h^{\bullet} concentrations in the studied system (*cf.* Cooper *et al.*, 2010). This hypothesis can be tested by performing simplified model calculations that consider the relative changes in melt composition on both sides of the diffusion couple as a function of distance to the interface, while ignoring simultaneous electron hole equilibration ($h^{\bullet}_{\text{equi}}$; see Fig. 3, Supplementary Information A.4.5). The estimated h^{\bullet} gradients predict an electron hole enrichment zone (oxidation) in the basaltic andesite near the interface, and an electron hole depletion zone (reduction) in the dacite, mimicking the measured redox variations. Here, the melt $\text{Fe}^{3+}/\Sigma\text{Fe}$ presumably responds immediately to the diffusion-induced electron hole imbalance, while the chemistry of the il-spl oxide pairs will follow those changes with a slight delay. Considering the small size of the oxides (typically $<5 \mu\text{m}$), equilibrium with the surrounding melt is reached within $\ll 10$ hr (Freer and Hauptman, 1978). Hence, the redox profiles determined for the basaltic andesite side of the diffusion couples may represent minimum gradients for the 1 hr and the 10 hr experiments, while it probably closely reflects the prevailing redox conditions of the melt in close proximity to the respective crystal pair for the 79 hr experiment. The proposed mechanism is consistent with theoretical considerations of Evans (2006) and studies of redox processes in Fe-bearing magnesium aluminosilicate glasses, and basaltic glasses and melts (*e.g.*, Cooper *et al.*, 1996, 2010).

We note that the release of predominantly ferrous Fe from resorbing cpx and opx (opx: Fe^{2+} ; cpx: low $\text{Fe}^{3+}/\Sigma\text{Fe}$) may decouple from the initial $f\text{O}_2$ and may contribute to the observed $\text{Fe}^{3+}/\Sigma\text{Fe}$ gradient on the dacitic side, but cannot explain the observed zigzag redox trend in full.

Implications of a Magma-Magma Mixing Redox Trap

The experiments show that a redox gradient can form when two chemically distinct magmas mix across an evolving compositional and textural interface. The net gradient, the stability of the gradient, as well as the spatial extent of the gradient are probably significantly affected by the (pre-)mixing pressure and temperature conditions as well as by the compositions and $f\text{O}_2$ of the two mixing magmas. Whether the observed effect of local magma reduction/oxidation is of

importance on a larger scale during magma evolution depends on the timescale of fractionation of melts and the surface area of mafic-felsic interfaces. It presumably affects redox conditions recorded by melt inclusions entrapped near the boundary during an initial stage of mixing.

We suggest that the observed redox process has implications for the mass transfer of S from mafic to felsic magma during underplating and/or recharge events. Here, S mass transfer occurs by diffusive transport or as a component of a magmatic volatile phase (MVP), and both mechanisms are dependent on the oxidation state of S (*e.g.*, Wallace, 2005; Behrens and Stelling, 2011; Audéat and Simon, 2012; Burgisser *et al.*, 2015; Parmigiani *et al.*, 2016). Although more experiments are required, we also presume variations in $f\text{O}_2$ at the magma-magma boundary layer under more reducing pre-mixing conditions, considering that the proposed mechanism, *i.e.* diffusion-induced electron hole imbalance, primarily depends on chemical differences, and less on the pre-mixing oxidation state of polyvalent elements (mainly Fe, S). In such systems, changes in the $\text{SO}_2/\text{H}_2\text{S}$ ratio of the MVP are expected near the magma-magma interface (*e.g.*, Burgisser *et al.*, 2015), modifying its ability to scavenge Au from the melt (Zajacz *et al.*, 2012). On the contrary, Cu exists in the MVP as a neutral Cu-alkali-Cl complex and its MVP/melt partitioning is redox insensitive (Zajacz *et al.*, 2012). Hence, the observed redox effects may moderate the Cu/Au ratio of porphyry-type ore deposits that ultimately form by advection of a MVP into the overlying environment (Audéat and Simon, 2012).

Acknowledgements

This project was supported by a US National Science Foundation Collaborative Research grant to A.C.S. (EAR 1250239) and P.R. (EAR 1250414). P.R. also acknowledges support through EAR 1347880. This research used resources of the Advanced Photon Source, a US Department of Energy (DOE) Office of Science User Facility operated for the DOE Office of Science by Argonne National Laboratory under Contract No. DE-AC02-06CH11357. Brief discussions with Paul Ratteron, Reid Cooper and Dave Walker were helpful to refine our model of the redox gradient. We are grateful to Bruno Scaillet, anonymous reviewers, and the editorial advice of Helen Williams who helped to improve this manuscript.

Editor: Helen Williams

Additional Information

Supplementary Information accompanies this letter at www.geochemicalperspectivesletters.org/article1722





This work is distributed under the Creative Commons Attribution 4.0 License, which permits unrestricted use, distribution, and reproduction in any medium, provided the original author and source are credited. Additional information is available at <http://www.geochemicalperspectivesletters.org/copyright-and-permissions>.

Cite this letter as: Fiege, A., Ruprecht, P., Simon, A. (2017) A magma mixing redox trap that moderates mass transfer of sulphur and metals. *Geochem. Persp. Let.* 3, 190–199.

References

- ANNEN, C., BLUNDY, J.D., SPARKS, R.S.J. (2006) The Genesis of Intermediate and Silicic Magmas in Deep Crustal Hot Zones. *Journal of Petrology* 47, 505–539.
- AUDÉTAT, A., SIMON, A. (2012) Magmatic controls on porphyry Cu genesis. In: Hedenquist, J.W., Harris, M., Camus, F. (Eds.) *Economic Geology Monograph in honor of Richard Sillitoe*. Society of Economic Geologists Special Publication No. 16, 553–572.
- BACON, C.R., HIRSCHMANN, M.M. (1988) Mg/Mn partitioning as a test for equilibrium between coexisting Fe-Ti oxides. *American Mineralogist* 73, 57–61.
- BACON, C.R., METZ, J. (1984) Magmatic inclusions in rhyolites, contaminated basalts, and compositional zonation beneath the Coso volcanic field, California. *Contributions to Mineralogy and Petrology* 85, 346–365.
- BEHRENS, H., STELLING, J. (2011) Diffusion and redox reactions of sulfur in silicate melts. *Reviews in Mineralogy and Geochemistry* 73, 79–111.
- BERGANTZ, G.W. (2000) On the dynamics of magma mixing by reintrusion: implications for pluton assembly processes. *Journal of Structural Geology* 22, 1297–1309.
- BURGISSER, A., ALLETTI, M., SCAILLET, B. (2015) Simulating the behavior of volatiles belonging to the C–O–H–S system in silicate melts under magmatic conditions with the software D-Compress. *Computers & Geosciences* 79, 1–14.
- COOK, G.B., COOPER, R.F. (2000) Iron concentration and the physical processes of dynamic oxidation in an alkaline earth aluminosilicate glass. *American Mineralogist* 85, 397–406.
- COOPER, R.F. (2017) Redox Thermodynamics and Kinetics in Silicate Melts and Glasses—and Related Morphology/Texture. In: Richet, P. (Ed.) *Encyclopedia of Glass Science, Technology, History and Culture*. In press.
- COOPER, R.F., FANSELOW, J.B., POKER, D.B. (1996) The mechanism of oxidation of a basaltic glass: chemical diffusion of network-modifying cations. *Geochimica et Cosmochimica Acta* 60, 3253–3265.
- COOPER, R.F., EVERMAN, R.L., HUSTOFT, J.W., DAN SHIM, S.H. (2010) Mechanism and kinetics of reduction of a FeO-Fe₂O₃-CaO-MgO aluminosilicate melt in a high-CO-activity environment. *American Mineralogist* 95, 810–824.
- DEPAOLO, D.J. (1981) Trace element and isotopic effects of combined wallrock assimilation and fractional crystallization. *Earth and Planetary Science Letters* 53, 189–202.
- EVANS, K.A. (2006) Redox decoupling and redox budgets: Conceptual tools for the study of earth systems. *Geology* 34, 489–492.
- FIEGE, A., RUPRECHT, P., SIMON, A.C., BELL, A.S., GÖTTLICHER, J., NEWVILLE, M., LANZIROTTI, T., MOORE, G. (2017) Calibration of Fe XANES for high-precision determination of Fe oxidation state in glasses: Comparison of new and existing results obtained at different synchrotron radiation sources. *American Mineralogist* 102, 369–380.



- FREER, R., HAUPTMAN, Z. (1978) Experimental-study of magnetite-titanomagnetite interdiffusion. *Physics of the Earth and Planetary Interiors* 16, 223–231.
- GAILLARD, F., SCHMIDT, B., MACKWELL, S., MCCAMMON, C. (2003) Rate of hydrogen–iron redox exchange in silicate melts and glasses. *Geochimica et Cosmochimica Acta* 67, 2427–2441.
- GHIORSO, M.S., EVANS, B.W. (2008) Thermodynamics of Rhombohedral Oxide Solid Solutions and a Revision of the Fe-Ti Two-Oxide Geothermometer and Oxygen-Barometer. *American Journal of Science* 308, 957–1039.
- HILDRETH, W., MOORBATH, S. (1988) Crustal contributions to arc magmatism in the Andes of Central Chile. *Contributions to Mineralogy and Petrology* 98, 455–489.
- MORETTI, R. (2005) Polymerisation, basicity, oxidation state and their role in ionic modelling of silicate melts. *Annales Geophysicae* 48, 583–608.
- PARMIGIANI, A., FRAROUGH, S., HUBER, C., BACHMANN, O., SU, Y. (2016) Bubble accumulation and its role in the evolution of magma reservoirs in the upper crust. *Nature* 532, 492–495.
- PERUGINI, D., POLI, G., MAZZUOLI, R. (2003) Chaotic advection, fractals and diffusion during mixing of magmas: evidence from lava flows. *Journal of Volcanology and Geothermal Research* 124, 255–279.
- PICHAVANT, M., COSTA, F., BURGISSER, A., SCAILLET, B., MARTEL, C., POUSSINEAU, S. (2007) Equilibration Scales in Silicic to Intermediate Magmas Implications for Experimental Studies. *Journal of Petrology* 48, 1955–1972.
- PISTONE, M., BLUNDY, J.D., BROOKER, R.A. (2016) Textural and chemical consequences of interaction between hydrous mafic and felsic magmas: an experimental study. *Contributions to Mineralogy and Petrology* 171, 8.
- RUPRECHT, P., BACHMANN, O. (2010) Pre-eruptive reheating during magma mixing at Quizapu volcano and the implications for the explosiveness of silicic arc volcanoes. *Geology* 38, 919–922.
- RUPRECHT, P., BERGANTZ, G.W., DUFEK, J. (2008) Modeling of gas driven magmatic overturn: Tracking of phenocryst dispersal and gathering during magma mixing. *Geochemistry, Geophysics, Geosystems* 9, doi:10.1029/2008GC002022.
- WALLACE, P.J. (2005) Volatiles in subduction zone magmas: concentrations and fluxes based on melt inclusion and volcanic gas data. *Journal of Volcanology and Geothermal Research* 140, 217–240.
- WALLACE, P., GERLACH, T.M. (1994) Magmatic vapor source for sulfur dioxide released during volcanic eruptions: Evidence from Mount Pinatubo. *Science* 265, 497–499.
- WATSON, E.B. (1982) Basalt contamination by continental crust: Some experiments and models. *Contributions to Mineralogy and Petrology* 80, 73–87.
- ZAJACZ, Z., CANDELA, P.A., PICCOLI, P.M., WÄLLE, M., SANCHEZ-VALLE, C. (2012) Gold and copper in volatile saturated mafic to intermediate magmas: Solubilities, partitioning, and implications for ore deposit formation. *Geochimica et Cosmochimica Acta* 91, 140–159.
- ZHANG, Y., NI, H. (2010) Diffusion of H, C, and O Components in Silicate Melts. *Reviews in Mineralogy and Geochemistry* 72, 171–225.



■ A magma mixing redox trap that moderates mass transfer of sulphur and metals

A. Fiege^{4,5*}, P. Ruprecht⁶, A. Simon¹

Supplementary Information

The Supplementary Information includes:

- A. Methods and Extended Discussion
- B. Sample Registration
- C. EPMA, XANES, and Raman Data
- D. Phase Fractions of the Starting Materials and Experimental Run Products
- Figures S-A1 to S-A3 and Figure S-D1
- Tables S-A1 and S-A2, S-B1, S-C1 to S-C14, and S-D1 to S-D4

A. Methods and Extended Discussion

A.1 Experimental procedure

The experimental procedure is subdivided into three steps:

In the *first* step, two anhydrous glasses were produced from natural samples (Quizapu volcano, Chile; Ruprecht *et al.*, 2012) by using i) mafic enclaves with a basaltic andesite composition (VQ22A, IGSN: PPRAI100T) and ii) dacitic host rock (VQ37D, IGSN: PPRAI101I) and fusing the powdered rock at 1400 °C for 1 hr in a 1-atm. furnace (see Supplementary Information B for the full list of registered samples). The melts were quenched in a water bath, crushed and ground and fused again for 1 hr at 1400 °C to improve homogeneity. The short durations

and the fairly low temperatures minimise alkali loss, which was confirmed by X-ray fluorescence (XRF) bulk rock analyses prior to fusing and by EPMA of the anhydrous glasses after fusing (Table S-A1).

In the *second* step, hydrated, sulphur (S) and chlorine (Cl) bearing cylinders were prepared for each starting material. Anhydrous basaltic andesite and dacitic glass powder were each (separately) mixed thoroughly in an agate mortar with barite powder, which was used as the S source to add ~100 ppm S to the dacite and ~1000 ppm S to the basaltic andesite, respectively. De-ionised water and 10 % HCl_{aq} were used to add ~1.1 wt. % H₂O and ~500 ppm Cl to the basaltic andesite as well as ~3.9 wt. % H₂O and ~1500 ppm Cl to the dacite. The bulk water contents are sufficient to reach (near-)volatile saturated conditions in the dacite and the basaltic andesite at the experimental mixing temperature (= 1000 °C; see next step), considering the expected melt fraction (~20 % in the basaltic andesite and >95 % in the dacite; predicted by using MELTS; *cf.* Ghiorso and Sack, 1995); wherefore the intrinsic $fO_2 \approx$ the fO_2 within the capsule (*cf.* Jugo *et al.*, 2010). The basaltic andesite and the dacitic powder mixtures (~500 mg) were each loaded separately with de-ionised water and HCl_{aq} into a bottom welded (star crimped), 4.4 mm outer diameter (OD) and 4 mm inner diameter (ID) Au capsule. Gold was chosen as capsule material because it is known to take up negligible amounts of S and Fe at magmatic temperatures (*cf.* Ratajeski and Sisson, 1999; Zajacz *et al.*, 2012). The mixtures were compressed with a brass piston and a hammer and the capsules were welded shut. Each capsule was heated for >12 hr at 120 °C to check for leakage and to distribute the water homogeneously inside the capsule. The syntheses were conducted in vertical rapid-heat, rapid-quench, cold-seal TZM pressure vessels at 150 MPa using pure Ar gas as a pressure medium. The use of pure Ar results in an intrinsic redox of $\log(fO_2/\text{bar}) \approx \text{QFM} + 4 \pm 0.5$ at a water activity ($a(H_2O)$) of 1 (*e.g.*, Jugo *et al.*, 2010; Bell *et al.*, 2011 and references therein; Shea and Hammer, 2013). We ran the capsule containing the dacitic material for 4 days at 900 °C and the one with the basaltic andesite for 3 days at 1030 °C. Differences of $\log(fO_2/\text{bar})$ relative to the QFM buffer are given to specify fO_2 throughout the study unless otherwise mentioned. The thermal gradient within the vessel was calibrated to be less than 5 °C. Details about the starting material for the diffusion couple experiments (step 3) are given in Supplementary Information C (phase compositions) and D (phase fractions and map).

In the *third* step, the two capsules were sliced with a slow-speed diamond saw into ~4 mm long cylinders. Both cutting areas of these cylinders were polished, while the Au “shells” surrounding each cylinder were not removed, which preserves mechanical integrity during polishing. Three ~15 mm long Au tubes (ID ~4.75 mm) were sealed on one side with a Au lid. A brass piston was used to flatten the bottom. One basaltic andesite plus one dacite cylinder were loaded into each Au capsule, stacked vertically. The capsules were star crimped on top, while making sure that the two cylinders were in contact. After the capsules were welded shut, each capsule was loaded into a vertical TZM vessel and compressed to ~100 MPa. The pressure was released rapidly from the vessel by opening a manual valve. This procedure allowed us to check for leakage since

4. Earth and Environmental Sciences, University of Michigan, 1100 North University Ave, Ann Arbor, MI 48109-1005, USA

5. Earth and Planetary Sciences, American Museum of Natural History, Central Park West at 79th Street, New York, NY 10024-5192, USA

* Corresponding author (email: afiege@amnh.org)

6. Geological Sciences & Engineering, University of Nevada, 1664 N. Virginia Street, Reno, NV 89557, USA



an unsealed capsule would noticeably expand. It also insured firm contact of the two cylinders to allow direct interaction once the experiment was started. The capsules were re-loaded into the TZM vessel with the denser basaltic andesite below the dacite. The diffusion couple experiments were rapidly heated to 1000 °C by moving the sample with an electromagnet from the cold into the hot zone and run for 1, 10, and 79 hr at 150 MPa and QFM + 4 before isobaric rapid-quench. All runs were successful as confirmed by constant sample weights before and after the experiment. We want to note that our experiments were conducted at oxidising conditions, where all S is present as S⁶⁺, to minimise the complexity of these demanding experiments.

A.1.1 Selection of the volatile contents. The H₂O, S and Cl contents added to the basaltic andesite and to the dacite, respectively, were selected for the following reasons:

Water: The water contents added to the basaltic andesite (~1.1 wt. %) and to the dacite (~3.9 wt. %), respectively, were selected to reach volatile saturation on the mafic side and near-volatile saturation on the felsic side of the diffusion couple. Thus, the final water contents in both melts will be similar, limiting the transport of water between both charges. This is a geologically likely scenario for arc settings where mafic and felsic magmas are commonly hydrous (Grove *et al.*, 2012; Plank *et al.*, 2013) and the mafic magma often reaches volatile saturation during cooling near the interface (*e.g.*, Edmonds *et al.*, 2010). Here, the higher bulk volatile contents expected for the mafic endmember, when compared to our experiments, will mostly result in a higher fluid fraction affecting melt and mineral fractions and composition to a minor extent.

Sulphur: The S concentrations we added to both starting materials (basaltic andesite: 1000 ppm; dacite: 100 ppm) are reasonable considering the literature data for mafic and felsic melt inclusions (see *e.g.*, review of Wallace and Edmonds, 2011). Here, mafic magmas are known for their elevated S contents when compared to felsic magmas. This is one of the reasons why mafic magmas are often suggested to be the main source of S released during eruption of arc volcanoes (*e.g.*, Keppler *et al.*, 1999) and in ore deposits directly related to arc settings (*e.g.*, Mungall *et al.*, 2014).

Chlorine: Cl addition was motivated by our goal to explore conditions close to nature. Melts of mafic and felsic magmas typically contain hundreds to thousands of ppm of Cl (*e.g.*, Rutherford and Devine, 1996; Humphreys *et al.*, 2009). Here, Cl contents can be higher in the mafic or in the felsic melt, making the added Cl contents reasonable (basaltic andesite: 500 ppm; dacite: 1500 ppm). Considering that Cl is a non-redox sensitive, minor element in both systems, Cl is of lower importance for this study, which focuses on redox evolution near the magma-magma interface; hence, the Cl trends are not discussed.

Table S-A1 Composition of the bulk rock starting material and the anhydrous starting glass.

[wt. %]	Dacite (VQ-07-37D)		Basaltic andesite (VQ-06-22A)	
	bulk rock (a)	glass (b)	bulk rock (a)	glass (b)
SiO ₂	66.41	67.87 (0.39)	53.85	53.91 (0.37)
TiO ₂	0.540	0.55 (0.03)	0.996	1.00 (0.03)
Al ₂ O ₃	15.50	15.57 (0.12)	17.95	17.75 (0.16)
Fe ₂ O ₃ (tot)	3.27	3.50 (0.14)	8.46	8.63 (0.23)
MnO	0.087	0.06 (0.07)	0.133	0.12 (0.07)
MgO	0.86	0.89 (0.04)	4.76	4.84 (0.11)
CaO	2.36	2.41 (0.04)	7.95	8.13 (0.06)
Na ₂ O	5.15	5.40 (0.17)	3.81	3.98 (0.16)
K ₂ O	3.28	3.30 (0.03)	1.19	1.13 (0.03)
P ₂ O ₅	0.140	0.15 (0.03)	0.209	0.21 (0.06)
Cl	0.08	0.044 (0.005)	N.A.	0.013 (0.005)
Total	97.59	99.75 (0.50)	99.32	99.72 (0.57)

(a) Analysed *via* XRF at GeoAnalyticalLab, Washington State University, see Ruprecht *et al.* (2012).

(b) Analysed *via* EMP; 1 sigma standard deviation is given in parentheses; N = 25.

N.A.: Not analysed.

A.2 Analytical procedure

A.2.1 Electron probe microanalyses (EPMA). We measured glass and mineral compositions *via* electron probe microanalyses (EPMA) using the Cameca SX100 at the University of Michigan and at the American Museum of Natural History (AMNH) in New York. The full analytical procedures are provided in Supplementary Information C (Tables S-C1 and S-C6). The NIST (U.S. National Institute of Standards and Technology) reference glass SRM-610 was measured during glass analyses of each microprobe session to monitor the accuracy of the measurements and the relative deviation of the measured major element concentrations from the reported values (*e.g.*, Evans *et al.*, 2008; Guillong *et al.*, 2008; Webster *et al.*, 2009) was typically <5 %. Similar relative deviation of the measured major element concentrations from reported values (<5 %) was observed for mineral reference materials (Aug164905 - NMNH 164905, Jarosewich *et al.*, 1987; Ol174.1, White, 1966; San Carlos - USNM 111312/444, Jarosewich *et al.*, 1980) during the measurements of the pyroxenes and oxides in our run products.

Glass transects were measured from the top of the capsule in the dacite to the interface (Tables S-C3 to S-C5). The line transects were positioned near the centre of the capsule and perpendicular to the interface. The glass analyses



were challenging on the basaltic andesite side of the diffusion couple owing to the high crystallinity (typically >75 %) and small melt pockets (often less than 20 μm in diameter). Here, a contribution of crystalline phases to some of the glass measurements cannot be entirely ruled out and the glass compositions of the basaltic andesite have to be interpreted with caution.

We determined Fe-Ti oxide compositions in the basaltic andesite near the centre of the capsule and perpendicular to the interface (Table S-C9). Spinels (spl) and rhombohedral oxides (for simplicity referred to as ilmenite, il, hereafter) were measured in close proximity (typically <50 μm apart from each other relative to the interface). Touching spl-il pairs were analysed whenever possible and oxide pairs were only considered when in Mg/Mn equilibrium (Bacon and Hirschmann, 1988). The oxides are small (<10 μm) with il commonly <5 μm in diameter. Thus, measurements were conducted by manually controlling the stage and varying the beam current (10–20 nA). Contributions by other phases were noticed for some analyses in particular in high CaO and SiO₂ contents. The small ilmenites made high quality quantitative analyses challenging. We therefore include all analyses with total sums of 100 ± 2.5 wt. % in our discussion and data tables. Compositional trends in the oxides (see Fig. 2) are robust when all these analyses are included. Ti patterns in spinels within the basaltic andesite are robust when further limiting the accepted data quality ($100 + 1$ wt. %), while a significant number of ilmenite analyses would have to be discarded for such a stringent quality cut-off.

Pyroxene compositions were obtained for the largest crystals without observing systematic variation either among or within experimental charges (Tables S-C7 and S-C8). We measured most pyroxenes for the longest duration experiment (A3D3-2). The quantitative analyses were performed at a range of beam currents (5–20 nA) to minimise the excitation volume and the contamination of the analyses from other phases. However, most analyses show minor contributions from glass indicated by correlated and high concentrations of Al₂O₃ and Na₂O limiting the use of geothermobarometers to check for equilibrium.

Semi-quantitative analyses *via* energy dispersive X-ray spectroscopy (EDS) using an EVO 60 Zeiss scanning electron microscope (SEM) at the AMNH were obtained for plagioclase (plg) in all samples.

The run products of the diffusion couple experiments were mapped across the interface (about ± 250 μm ; Figs. 1 and S-A1). The five wavelength dispersive X-ray spectroscopy (WDS) spectrometers of the Cameca SX100 were used to measure Al, Fe, Mg, Ca and K while an EDS detector was used to detect counts for Si and Na (conditions: acceleration voltage: 15 keV; beam current: 30 nA; focused beam). The step size was 1 μm and the dwell time was 0.1 s. The counts per point for each element were used to calculate phase assemblage maps using a processing script written in MATLAB by MathWorks (Tables S-D2 to S-D4). The different phases were unequivocally identified in the elemental maps (Mg: orthopyroxene, opx; Ca: clinopyroxene, cpx; Fe: oxides; Al: plg; K: glass). A distinction between spl and il within the maps is not possible. Uncertainties in the

fraction of the different phases are mainly due to small crystal sizes in the experimental run products (typically <10 μm). While the unique chemical signatures of opx, cpx and oxides make their identification robust using unique thresholds for the gray values of the specific element maps, larger absolute uncertainties (estimated to be within 20 % absolute) arise from the compositional similarities of glass and plg. The processed maps were also used to extract the fraction of each phase present at a given distance away from the interface (Fig. 1). High-resolution BSE images (2,000–3,000 \times magnification) from various locations throughout the charges were processed to confirm locally the phase fractions. A full summary of the phase fraction estimates is provided in Supplementary Information D.

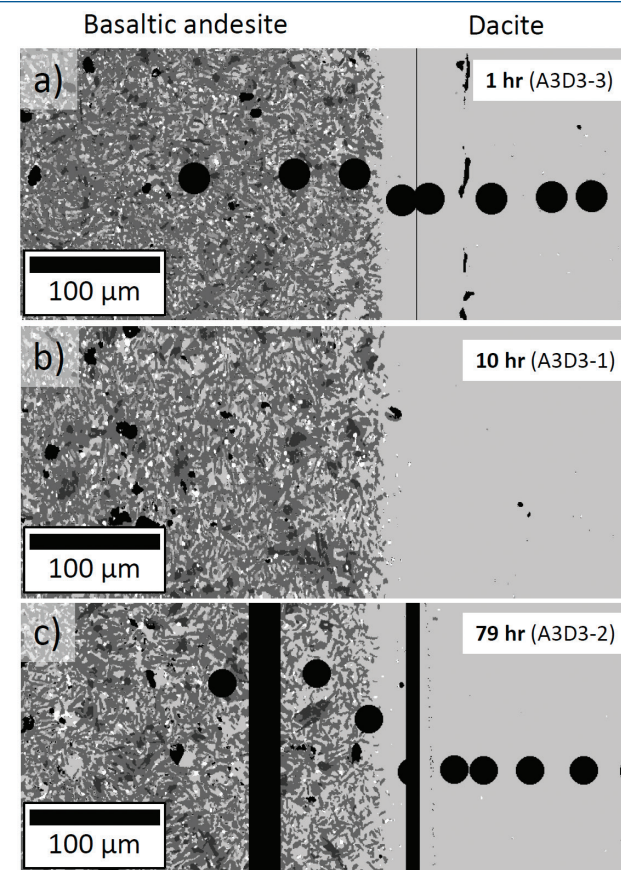


Figure S-A1 Back scattered electron (BSE) images of the run products of the diffusion couple experiments.



A.2.2 Micro X-ray absorption near-edge structure analyses. Micro X-ray absorption near-edge structure (μ -XANES) spectroscopy analyses at Fe K-edge were performed on each of the experimental dacitic glasses from the three diffusion couple experiments *via* line transects from the magma-magma interface into the dacite to determine the Fe oxidation state in the dacitic glasses. These transects were positioned perpendicular to the interface and extend ≥ 750 μm away from it. Micro-XANES analyses of the glass on the mafic side of the diffusion couple were not attempted, owing to the high crystallinity of the basaltic andesite (*i.e.* small melt pockets) and the difficult identification of melt pockets through reflected light and X-ray maps. The measurements were conducted at the GSECARS 13-ID-E beamline of the Advanced Photon Source (APS, Argonne, USA). APS operates at an energy of 7 GeV and a beam current of 100 mA, at which the electrons are injected into a 1104 m circumference storage ring. The 13-ID-E beamline allows a high spatial resolution by focusing the beam down to $2 \mu\text{m} \times 1 \mu\text{m}$ by using Kirkpatrick-Baez focusing mirrors. We followed the approach described by Fiege *et al.* (2017). The energy of the first derivative peak of Fe metal foil was calibrated to the Fe K-edge energy of 7110.75 eV as determined by Kraft *et al.* (1996). The spectra were collected in fluorescence mode (in/out angle: 45°) from 7062 to 7312 eV (total number of points per spectra: 399; counting time per point: 1 s; step size: 5 eV from 7062 to 7107 eV; 0.1 eV from 7107 to 7137 eV (pre-edge region); ~ 2 eV from 7137 to 7312 eV).

The software Athena (Ifeffit package; Newville, 2001) was used to pre-edge/post-edge normalise the spectra. The pre-edge peak was fit from ~ 7082 to ~ 7119 eV by using an exponentially modified Gaussian and an arctangent function for the background and two Gaussians to fit pre-edge peak. Here, we used the programme Fityk (Wojdyr, 2010) to fit the background and the pre-edge feature (see Fiege *et al.*, 2017).

A self-absorption (SA) correction of the raw μ -XANES spectra was not applied because SA has a negligible influence on the centroid energy (*cf.* Cottrell *et al.*, 2009) and SA correction algorithms yielded no satisfactory results for the experimental glasses (see also Botcharnikov *et al.*, 2005). Thus, instead of using the equation provided by Fiege *et al.* (2017) for rhyolitic glasses, we used SA uncorrected spectra collected on the same set reference glasses for the calibration. In Table S-A2 we list the measured centroid energies for the reference glasses. The regression (Eq. S-A1) was fit by using the software KaleidaGraph and applying the locally weighted least squared error method and a 2σ error for the centroid energy (Fig. S-A2).

$$C_{\text{Fe}} [\text{eV}] = 0.010303 (\pm 0.00005298) \cdot \text{Fe}^{3+}/\Sigma\text{Fe} + 7112.2 (\pm 0.0016771); R^2 = 0.998,$$

Eq. S-A1

This equation is based on the analyses of 19 felsic glasses with known Fe oxidation state (60.9 to 77.5 wt. % SiO_2 ; 1.3 to 5.7 wt. % FeO_{tot}). No beam damage was observed (for details see Fiege *et al.*, 2017).

Table S-A2 Centroid energies of the Fe pre-edge peak determined for felsic reference glasses.

Sample ID	$\text{Fe}^{3+}/\Sigma\text{Fe}$ [%]	C_{Fe} [eV]
Rhyolite		
DT-18-a	66	7112.863
DT-18-b	66	7112.859
DT-29-a	80.6	7112.991
DT-29-b	80.6	7113.066
DT-31	63	7112.780
DT-39	31.5	7112.453
DT-46-a	56.9	7112.782
DT-46-b	56.9	7112.764
VG568-a	23.8	7112.413
VG568-b	23.8	7112.374
H2O-52	54.9	7112.753
H2O-53	50.1	7112.759
H2O-54	56.2	7112.883
H2O-55	57.2	7112.734
H2O-63-a	59.6	7112.825
H2O-63-b	59.6	7112.839
H2O-66	53.5	7112.769
H2O-67	59.7	7112.785
REV-1	28.1	7112.532
REV-3	51.3	7112.724
Dacite		
PD2K3-a	27	7112.423
PD2K3-b	27	7112.405
PD2K4-a	23	7112.401
PD2K4-b	23	7112.356
Andesite		
AH	34	7112.472
SD1	39	7112.551

Average 2σ errors: centroid energies: ± 0.04 eV; $\text{Fe}^{3+}/\Sigma\text{Fe}$: ± 2 %.

See Fiege *et al.* (2017) for details about the reference glasses. Some of the reference glasses (7) were analysed on a sample mount (NMNH 117436) loaned to us by the Smithsonian Institution (National Museum of Natural History, Washington, DC, USA).



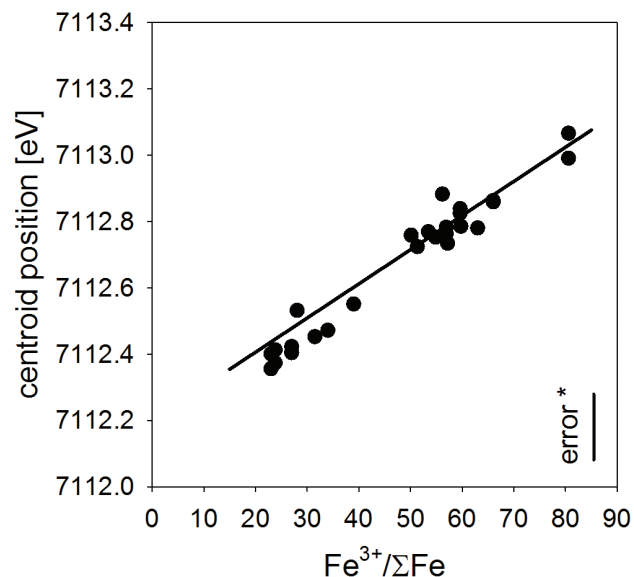


Figure S-A2 Results of the Fe μ -XANES calibration. The solid line represents the linear regression (Eq. S-A1). *conservative estimation for the overall analytical uncertainty of the Fe μ -XANES method (see Cottrell *et al.*, 2009; Fiege *et al.*, 2017).

A.3 Starting compositions

A.3.1 Phase assemblage prior to mixing. The phases in the basaltic andesite prior to mixing were identified in order of abundance as plg (46.6 ± 3.0 %; An_{48±3}; compositions estimated by EDS), glass (24.6 ± 4.4 %), opx (12.9 ± 2.0 %; Mg#_{84±2}), cpx (10.6 ± 1.0 %; Fs_{11±2} En_{49±3} Wo_{40±4}), oxides (spl + il = 4.9 ± 0.5 %) and vesicles (0.4 ± 0.4 %). Prior to mixing, the dacite is predominantly glassy (86.6 ± 3.9 %) with minor plg (8.9 ± 3.4 %; An_{35±5}) as well as accessory hornblende (hbl; 1.7 ± 0.5 %; identified *via* EDS), oxides (1.6 ± 0.2 %), opx (0.8 ± 0.5 %; Mg#_{88±1}), and vesicles (0.4 ± 0.2 %). Considering the run durations (3–4 days), these phase assemblages presumably represent equilibrium conditions for the dacite at 900 °C and for the basaltic andesite at 1030 °C.

A.4 Extended results and discussion

A.4.1 Presence/absence of a fluid phase in the diffusion couple experiments.

The dacite is vesicle-free, mainly due to the resorption of plg during heating from 900 to 1000 °C, whereas the basaltic andesite contains some vesicles, indicating that the basaltic andesite magma is volatile saturated. These vesicles only occur in areas of the basaltic andesite that are not yet significantly affected by

the mixing process with the dacite; *i.e.* where the melt fraction is still very low (~20 %; Fig. 1 and Supplementary Information A.2). A glass fraction of 20 % on the basaltic andesite side implies a H₂O content in the residual melt of ~5.5 wt. %, considering the bulk H₂O content of the basaltic andesite. The H₂O solubility in the basaltic andesite melts at 150 MPa and 1000 °C is slightly lower (3.8 to 4.0 wt. %; *e.g.*, *VolatileCalc*, Newman and Lowenstern, 2002). On the other hand, the dacite is almost crystal-free, leading to a water content in the melt of ~3.9 wt. %, which is slightly below the expected H₂O solubility of ~4.5 wt. % in the dacitic melts at the prevailing pressure-temperature conditions (*VolatileCalc*). Hence, the observations of near-volatile saturated basaltic andesites and slightly water undersaturated dacites are consistent with the bulk H₂O added to each system and predicted H₂O solubilities. This indicates that $a(\text{H}_2\text{O})$ is near 1 throughout each of the three charges, considering that the fluid phase on the basaltic andesite side predominantly contains water (see *e.g.*, model by Burgisser *et al.*, 2015). Furthermore, these calculations indicate that there is probably little to no H₂O gradient between the melt fractions on both sides of the interface. The absence of a H₂O gradient is in agreement with the EPMA data and Raman spectra collected on the dacitic side (see Supplementary Information C; *e.g.*, plots near Table S-C14a,b). Notably, the variable EPMA totals observed on the basaltic andesite side are interpreted to reflect variable contributions of anhydrous phases to the spot analyses due to the small melt pools. Thus, diffusive transport of H₂O can be ruled out as a reason for the redox gradients near the interface.

A.4.2 Possible upward migration of a fluid phase. Based on microscopic investigations, BSE imaging (Fig. S-A1) and WDS/EDS mapping (Fig. 1) it becomes clear that the basaltic andesite is volatile saturated (vesicles present), while the dacite is not (vesicles absent). This is in agreement with mass balance calculations, EPMA data and Raman spectra (see above).

Regarding sulphur transfer within the charge, in two out of three run products of our experiments we observe spikes in the S content in the dacitic melt (see Tables S-C3 to S-C5), reaching concentrations of almost 450 ppm, whereas the average S content in the far field of the dacite is about 100 ppm S. We interpret this observation as an experimental artefact, which may have implications for natural systems. Micro cracks may be produced when the synthesised cylinders of the mafic and felsic starting materials are sliced using a Buehler low-speed saw equipped with diamond wafering blade (experimental *step* 3). These cracks presumably heal fast once the high P-T diffusion couple experiment is started. However, during rapid heating there might be a short time frame, which allows exsolved fluids from the basaltic andesite to migrate upwards and into the dacite through not yet fully healed cracks. Such an experimental artefact is not of relevance for the observed redox gradient since nowhere in the diffusion couple experiments do fO₂ gradients result in the formation of sulphide in the melt (confirmed by μ -XANES at S k-edge; see also Jugo *et al.*, 2010). On the other hand, it has been proposed that rapid fluid transport can be facilitated through hydraulic tensile fracturing (Hautmann *et al.*, 2014) or *via* viscous fingering



(Parmigiani *et al.*, 2016). Although the fractures in our experiments originate from a totally different process, they might be interpreted as supporting evidence for this mechanism of rapid fluid transport.

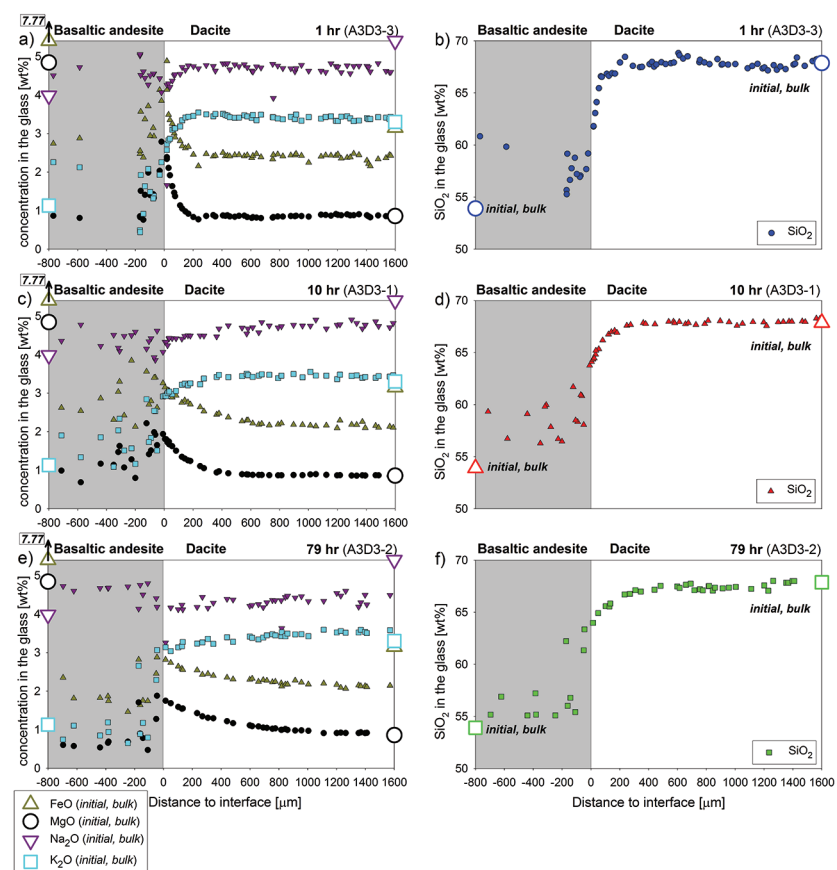


Figure S-A3 FeO, MgO, Na₂O, K₂O and SiO₂ concentration profiles measured *via* EPMA in the glasses of the diffusion couple experiments. (a–b) 1 hr run duration (experiment A3D3-3). (c–d) 10 hr (A3D3-1). (e–f) 79 hr (A3D3-2). The larger, open symbols (with coloured edges) mark the initial contents measured in the anhydrous dacitic and basaltic andesite starting glasses. The black arrows indicate that the initial FeO_{tot} content of the anhydrous basaltic andesite glass was 7.77 wt. % (see Table S-A1). The 1 σ error of the presented oxide concentrations are: ± 0.2 wt. % FeO; ± 0.1 wt. % MgO; ± 0.2 wt. % Na₂O; ± 0.05 wt. % K₂O; ± 0.4 wt. % SiO₂. The error of the distance is smaller than symbol size.

A.4.3 Major element compositions in diffusion couple experiments. All profiles within the dacitic side of the diffusion couple are smooth and flatten out with experimental duration (Fig. S-A3). Element concentrations in the melt on the basaltic andesite side show more scatter, probably related to small contributions of mineral phases to the EPMA, but on average remain rather constant. Except for the Na content in the dacitic glasses of the diffusion couple experiments, the differences between the bulk contents of the anhydrous starting glass and the far side of the dacite and the basaltic andesite can be explained by the presence of mineral phases, such as oxides that lower the FeO content in the melt upon crystallisation. The slightly lower Na content at the far side of the dacite when compared to the bulk Na content is probably related to the loss of some Na to a Cl-containing fluid phase during the synthesis of the dacitic starting material at 900 °C; *i.e.* the dacite is presumably volatile saturated at 900 °C (see map of QD3, Supplementary Information D) and this fluid is partly lost during the preparation of the diffusion couple capsules. The far side of the basaltic andesite is characterised by a slightly higher crystallinity (~80 %) when compared to hydrated starting material (~75 %), owing to the slight differences in temperature between the two steps (1000 *vs.* 1030 °C).

A.4.4 Calculation of the local redox conditions in the dacite and the basaltic andesite. We link the μ -XANES data to the nearest EPMA glass analyses for the calculations. On average μ -XANES measurements are ~16 μ m away from the nearest EPMA data point relative to the interface. Given the smooth change in glass compositions within the dacite glass uncertainties resulting from small mismatches between μ -XANES and EPMA measurement locations are negligible. We calculate local redox conditions using the model of Moretti (2005), which considers, *e.g.*, the influence of pressure, temperature, and melt composition (including H₂O) on the relationship between fO_2 and Fe³⁺/ Σ Fe. We note that diffusion-induced electron hole imbalance presumably results in an almost instantaneous change of the local Fe speciation *via* localised electron transfer, wherefore the thermodynamic models simulating equilibrium conditions (*e.g.*, the Fe oxidation state model by Moretti, 2005) can be applied to estimate the local redox (fO_2) in our run products.

We were able to collect two μ -XANES spectra on the basaltic andesite side of the 10 hr diffusion couple experiment (distance to the interface: -8 and -22 μ m; Table S-C12), which indicate an about one log unit lower fO_2 as determined *via* two-oxide oxybarometry at a similar position. This confirms the slightly delayed response of the oxides to changes in redox in the melt (see Discussion of the Redox Mechanism, main text).

It has been shown previously that the two-oxide model recovers the absolute fO_2 values to better than 1 log unit (Fig. 27 of Ghiorso and Evans, 2008), even for the most oxidising conditions, which fall above the model calibrated range of Δ NNO \pm 3 (NNO: nickel-nickel oxide buffer). The relative variations within one sample are much more precise (± 0.25 log units fO_2 , 2 σ) as they mostly depend on the analytical uncertainties of the Ti and Fe determinations in the oxides and



that precision is comparable to fO_2 values determined *via* Fe μ -XANES, which is <0.3 log units (*cf.* Cottrell *et al.*, 2009). At large distances from the interface both redox trends (μ -XANES and two-oxides) match within error the intrinsic redox of both the TZM apparatus ($-QFM + 4$ at $a(H_2O) = 1$) of the diffusion couple experiments and the fO_2 set in *step 2* of the experimental procedure for the starting basaltic andesite and dacite, providing independent constraints that the calculated variations in fO_2 are accurate. Notably, the fO_2 inside a capsule is a function of $a(H_2O)$, where $\log(fO_2)^{capsule} = \log(fO_2)^{at\ a(H_2O)=1} + 2 \log(a(H_2O))$; for details see Berndt *et al.* (2002), Jugo *et al.* (2010). As mentioned above (Section A.4.1), $a(H_2O)$ is estimated to be near 1 throughout each experiment, wherefore the vessel imposed $\log(fO_2)$ inside the capsules is about $QFM + 4$.

A.4.5 Extended discussion of the redox gradients. Despite the tremendously close match in profile shape, the calculated *maximum* electron hole imbalance would allow the oxidation/reduction of up to 10 wt. % Fe near the interface, while we observe a maximum change by ~ 0.8 wt. % Fe. The main reason for this discrepancy is probably that we do not account for the effects of simultaneous electron hole equilibration (h^*_{equi}). The counter flux of electron holes between the dacite and the basaltic andesite is probably balancing most of the potential redox effect imposed by chemical exchange between the two systems (*e.g.*, Cook and Cooper, 2000; Gaillard *et al.*, 2003). Furthermore, contrasting our calculations, not all diffusing species in a magma-magma diffusion couple may contribute equally based on their charges to a potential electron hole gradient. A more robust model should perhaps consider local changes in melt structure and possibly weigh the contribution of the diffusing species (*i.e.* divalent network modifying cations are probably the main redox carriers; *cf.* Cooper, 2017). In addition, the fO_2 imposed by the vessel continuously re-equilibrates the fO_2 inside the capsule as indicated by the fading T effect on fO_2 (*e.g.*, Fig. 2, main text), and by the decreasing fO_2 gradient on the dacitic side. This is supported by Fe μ -XANES analyses on the dacitic side ~ 170 μm away from the interface close to the capsules wall. These analyses record $Fe^{3+}/\Sigma Fe$ ratios identical within error with those measured in the centre of the charge after 1 hr (~ 0.69 in the centre *vs.* ~ 0.72 at the wall), but significantly higher than those observed after 10 hr (~ 0.55 *vs.* ~ 0.76) and 79 hr (~ 0.61 *vs.* ~ 0.70). The transport of H_2 *via* diffusion through the basaltic andesite is limited owing to the high crystallinity. This explains why the redox gradient is slowly increasing on the basaltic andesite side, while it is rather fading with experimental run duration on the dacitic side. Such vessel effects may also be responsible for the small profile variations in all three time-series experiments. Notably, the fO_2 in the capsules are indirectly adjusted *via* the diffusion of H_2 through the capsule wall and the reaction with H_2O ($H_2 + \frac{1}{2} O_2 \leftrightarrow H_2O$; *e.g.*, Berndt *et al.*, 2002). Hydrogen diffusion through the Au capsule wall is fast and should not be a limiting factor for redox equilibration between the vessel and the material inside the capsule (*e.g.*, Chou, 1986; Bell *et al.*, 2011). The latest model for H_2 diffusion in silicate melts predicts an almost 3 orders of magnitude faster hydrogen transport through the melt than Fe ($\log(D_{H_2}) \approx -9.0$ m^2/s , $x \approx \sqrt{(D_{H_2} \cdot t)} \approx 1.9$ mm (1 hr), 6.1 mm (10 hr), 17 mm (79 hr); Zhang and Ni, 2010).

A transient redox gradient forming at the interface during magma-magma mixing under more reducing conditions may be less distinct or steady owing to the higher partial H_2 pressure in such systems (*i.e.* the net H_2 supply/discard is higher). Moreover, the oxide dissolution near the interface can partly explain the discrepancies between the calculated maximum electron hole gradients and measured redox gradients as their dissolution slightly compensates redox gradients. However, reduction of the dacite near the interface is manifested despite the potential buffering *via* the vessel and *via* spl dissolution at relatively high temperature of ~ 1000 °C. We emphasised that such mixing temperatures (T_M) are high but reasonable (Ruprecht and Bachmann, 2010) and can be reached if the mass ratio of a “hot” basaltic magma intruding into a magma chamber of “colder” felsic host magma is relatively high; *e.g.*, a T_M of ~ 1000 °C is reached if 850 °C dacite is interacting with equal amounts of 1150 °C basalt assuming that heat capacities of the melts are equal and that non-equilibrium effects causing the preferential release (dissolution) or consumption (crystallisation) of latent heat are negligible. However, such latent heat effects can be significant and may considerably reduce the mafic recharge volume required to reach $T_M = 1000$ °C (Ruprecht and Bachmann, 2010).

Supplementary information A references

- BACON, C.R., HIRSCHMANN, M.M. (1988) Mg/Mn partitioning as a test for equilibrium between coexisting Fe-Ti oxides. *American Mineralogist* 73, 57–61.
- BELL, A. S., SIMON, A., GUILLONG, M. (2011) Gold solubility in oxidized and reduced, water-saturated mafic melt. *Geochimica et Cosmochimica Acta* 75, 1718–1732.
- BERNDT, J., LIEBSKE, C., HOLTZ, F., FREISE, M., NOWAK, M., ZIEGENBEIN, D., HURKUCK, W., KOEPKE, J. (2002) A combined rapid-quench and H_2 -membrane setup for internally heated pressure vessels: description and application for water solubility in basaltic melts. *American Mineralogist* 87, 1717–1726.
- BOTCHARNIKOV, R.E., KOEPKE, J., HOLTZ, F., MCCAMMON, C., WILKE, M. (2005) The effect of water activity on the oxidation and structural state of Fe in a ferro-basaltic melt. *Geochimica et Cosmochimica Acta* 69, 5071–5085.
- BURGISSER, A., ALLETTI, M., SCAILLET, B. (2015) Simulating the behavior of volatiles belonging to the C–O–H–S system in silicate melts under magmatic conditions with the software D-Compress. *Computers & Geosciences* 79, 1–14.
- CHOU, I.M. (1986) Permeability of precious metals to hydrogen at 2 kb total pressure and elevated temperatures. *American Journal of Science* 286, 638–658.
- COOK, G.B., COOPER, R.F. (2000) Iron concentration and the physical processes of dynamic oxidation in an alkaline earth aluminosilicate glass. *American Mineralogist* 85, 397–406.
- COOPER, R.F. (2017) Redox Thermodynamics and Kinetics in Silicate Melts and Glasses—and Related Morphology/Texture. In: Richet, P. (Ed.) *Encyclopedia of Glass Science, Technology, History and Culture*. In press.
- COTTRELL, E., KELLEY, K.A., LANZIROTTI, A., FISCHER, R.A. (2009) High-precision determination of iron oxidation state in silicate glasses using XANES. *Chemical Geology* 268, 167–179.
- EDMONDS, M., AIUPPA, A., HUMPHREYS, M., MORETTI, R., GIUDICE, G., MARTIN, R.S., HERD, R.A., CHRISTOPHER, T. (2010) Excess volatiles supplied by mingling of mafic magma at an andesite arc volcano. *Geochemistry, Geophysics, Geosystems* 11, Q04005, doi: 10.1029/2009GC002781.



- EVANS, K.A., O'NEILL, H.S.C., MAVROGENES, J.A. (2008) Sulphur solubility and sulphide immiscibility in silicate melts as a function of the concentration of manganese, nickel, tungsten and copper at 1 atm and 1400 °C. *Chemical Geology* 255, 236–249.
- FIGE, A., RUPRECHT, P., SIMON, A.C., BELL, A.S., GÖTTLICHER, J., NEWVILLE, M., LANZIROTTI, T., MOORE, G. (2017) Calibration of Fe XANES for high-precision determination of Fe oxidation state in glasses: Comparison of new and existing results obtained at different synchrotron radiation sources. *American Mineralogist* 102, 369–380.
- GAILLARD, F., SCHMIDT, B., MACKWELL, S., MCCAMMON, C. (2003) Rate of hydrogen-iron redox exchange in silicate melts and glasses. *Geochimica et Cosmochimica Acta* 67, 2427–2441.
- GHIORSO, M.S., EVANS, B.W. (2008) Thermodynamics of rhombohedral oxide solid solutions and a revision of the Fe-Ti two-oxide geothermometer and oxygen-barometer. *American Journal of Science* 308, 957–1039.
- GHIORSO, M.S., SACK, R.O. (1995) Chemical Mass Transfer in Magmatic Processes IV. A revised and internally consistent thermodynamic model for the interpolation and extrapolation of liquid-solid equilibria in magmatic systems at elevated temperatures and pressures. *Contributions to Mineralogy and Petrology* 119, 197–212.
- GROVE, T.L., TILL, C.B., KRAWCZYNSKI, M.J. (2012) The role of H₂O in subduction zone magmatism. *Annual Review of Earth and Planetary Sciences* 40, 413–439.
- GUILLONG, M., LATKOCZY, C., SEO, J.H., GUNTHER, D., HEINRICH, C.A. (2008) Determination of sulfur in fluid inclusions by laser ablation ICP-MS. *Journal of Analytical Atomic Spectrometry* 23, 1581–1589.
- HUMPHREYS, M.C., CHRISTOPHER, T., HARDS, V. (2009) Microlite transfer by disaggregation of mafic inclusions following magma mixing at Soufrière Hills volcano, Montserrat. *Contributions to Mineralogy and Petrology* 157, 609–624.
- KRAFT, S., STÜMPPEL, J., BECKER, P., KUETGENS, U. (1996) High resolution x ray absorption spectroscopy with absolute energy calibration for the determination of absorption edge energies. *Review of Scientific Instruments* 67, 681–687.
- JAROSEWICH, E., NELEN, J.A., NORBERG, J.A. (1980) Reference Samples for Electron Microprobe Analysis. *Geostandards Newsletter* 4, 43–47, doi: 10.1111/j.1751-908X.1980.tb00273.x.
- JAROSEWICH, E., GOOLEY, R., HUSLER, J. (1987) Chromium Augite - A New Microprobe Reference Sample. *Geostandards Newsletter* 11, 197–198, doi: 10.1111/j.1751-908X.1987.tb00027.x.
- JUGO, P.J., WILKE, M., BOTCHARNIKOV, R.E. (2010) Sulfur K-edge XANES analysis of natural and synthetic basaltic glasses: Implications for S speciation and S content as function of oxygen fugacity. *Geochimica et Cosmochimica Acta* 74, 5926–5938.
- MORETTI, R. (2005) Polymerisation, basicity, oxidation state and their role in ionic modelling of silicate melts. *Annals of Geophysics* 48, 583–608.
- NEWMAN, S., LOWENSTERN, J.B. (2002) VolatileCalc: a silicate melt–H₂O–CO₂ solution model written in Visual Basic for excel. *Computers & Geosciences* 28, 597–604.
- NEWVILLE, M. (2001) EXAFS data analysis program Athena. *Journal of Synchrotron Radiation* 8, 322.
- PARMIGIANI, A., FRAROUGH, S., HUBER, C., BACHMANN, O., SU, Y. (2016) Bubble accumulation and its role in the evolution of magma reservoirs in the upper crust. *Nature* 532, 492–495.
- PLANK, T., KELLEY, K.A., ZIMMER, M.M., HAURI, E.H., WALLACE, P.J. (2013) Why do mafic arc magmas contain ~4 wt. % water on average? *Earth and Planetary Science Letters*, *Frontiers Article Volume* 364, 168–179.
- RATAJESKI, K., SISSON, T.W. (1999) Loss of iron to gold capsules in rock-melting experiments. *American Mineralogist* 84, 1521–1527.
- RUPRECHT, P., BACHMANN, O. (2010) Pre-eruptive reheating during magma mixing at Quizapu volcano and the implications for the explosiveness of silicic arc volcanoes. *Geology* 38, 919–922.

- RUPRECHT, P., BERGANTZ, G.W., COOPER, K.M., HILDRETH, W. (2012) The Crustal Magma Storage System of Volcán Quizapu, Chile, and the Effects of Magma Mixing on Magma Diversity. *Journal of Petrology* 53, 801–840.
- RUTHERFORD, M.J., DEVINE, J.D. (1996) Pre-eruption pressure-temperature conditions and volatiles in the 1991 dacitic magma of Mount Pinatubo. In: Newhall, C.G., Punongbayan, R.S. (Eds.) *Fire and mud: eruptions and lahars of Mount Pinatubo, Philippines*. University of Washington Press, 751–766.
- WALLACE, P.J., EDMONDS, M. (2011) The sulfur budget in magmas: evidence from melt inclusions, submarine glasses, and volcanic gas emissions. *Reviews in Mineralogy and Geochemistry* 73, 215–246.
- WEBSTER, J.D., SINTONI, M.F., DE VIVO, B. (2009) The partitioning behavior of Cl, S, and H₂O in aqueous vapor- ± saline-liquid saturated phonolitic and trachytic melts at 200 MPa. *Chemical Geology* 263, 19–36.
- WHITE, R.W. (1966) Ultramafic inclusions in basaltic rocks from Hawaii. *Contributions to Mineralogy and Petrology* 12, 245–314.
- WOJDYR, M. (2010) Fityk: a general-purpose peak fitting program. *Journal of Applied Crystallography* 43, 1126–1128.
- ZAJACZ, Z., CANDELA, P.A., PICCOLI, P.M., SANCHEZ-VALLE, C. (2012) The partitioning of sulfur and chlorine between andesite melts and magmatic volatiles and the exchange coefficients of major cations. *Geochimica et Cosmochimica Acta* 89, 81–101.
- ZHANG, Y., NI, H. (2010) Diffusion of H, C, and O Components in Silicate Melts. *Reviews in Mineralogy and Geochemistry* 72, 171–225.

B. Sample Registration

Table S-B1 Sample registration.

IGSN	Sample Name	URL	Comment
PPRAI100T	VQ-06-22A	http://app.geosamples.org/sample/igs/PPRAI100T	Rock Sample - Andesite end-member
PPRAI101I	VQ-07-37D	http://app.geosamples.org/sample/igs/PPRAI101I	Rock Sample - Dacite end-member
PPRAI102L	A3D3-1	http://app.geosamples.org/sample/igs/PPRAI102L	10 hr diffusion-couple experiment
PPRAI102M	A3D3-2	http://app.geosamples.org/sample/igs/PPRAI102M	79 hr diffusion-couple experiment
PPRAI102N	A3D3-3	http://app.geosamples.org/sample/igs/PPRAI102N	1 hr diffusion-couple experiment
PPRAI102O	QA3	http://app.geosamples.org/sample/igs/PPRAI102O	Starting experimental charge - Andesite end-member
PPRAI102P	QD3	http://app.geosamples.org/sample/igs/PPRAI102P	Starting experimental charge - Dacite end-member



C. EMPA, XANES, and Raman Data

Supplementary Information C is available at <http://www.geochemicalperspectivesletters.org/article1722>.

Tables S-C1 to S-C5	EPMA conditions for glasses; composition of the glasses in the synthesised, hydrous starting materials QD3 (dacite) and QA3 (basaltic andesite), and results of the EPMA transects on the glasses of experiments A3D3-3 (1 hr), A3D3-1 (10 hr), and A3D3-2 (79 hr).
Tables S-C6 to S-C9	EPMA conditions for minerals, EPMA results for pyroxenes and oxides.
Table S-C10	Results of two-oxide oxybarometry.
Tables S-C11 to S-C13	Fe XANES results for experiments A3D3-3 (1 hr), A3D3-1 (10 hr), and A3D3-2 (79 hr).
Table S-C14	Raman data for experiments A3D3-3 (1 hr), A3D3-1 (10 hr), and A3D3-2 (79 hr).

D. Phase Fractions of the Starting Materials and Experimental Run Products

Supplementary Information D is available at <http://www.geochemicalperspectivesletters.org/article1722>.

Table S-D1	Phase fractions of the synthesised, hydrous starting materials QD3 (dacite) and QA3 (basaltic andesite).
Figure S-D1	Phase maps of the starting materials QD3 (dacite) and QA3 (basaltic andesite).
Tables S-D2 to S-D4	Phase fractions of the experiments A3D3-3 (1 hr), A3D3-1 (10 hr), and A3D3-2 (79 hr).

